Soft Matter

Accepted Manuscript

Volume 1 | Number 1 | Jan 2013 | Pages 1–100

Soft Matter

www.rsc.org/softmatter

ROYAL SOCIETY
OF CHEMISTRY

www.rsc.org/softmatter

Catalytic dimer nanomotors: continuum theory and microscopic dynamics

Shang Yik Reigh* **and Raymond Kapral***

Received Xth XXXXXXXXXX 20XX, Accepted Xth XXXXXXXXX 20XX
First published on the web Xth XXXXXXXXXX 200X
DOI: 10.1039/b000000x

Synthetic chemically-powered motors with various geometries have potentially new applications involving dynamics on very small scales. Self-generated concentration and fluid flow fields, which depend on geometry, play essential roles in motor dynamics. Sphere-dimer motors, comprising linked catalytic and noncatalytic spheres, display more complex versions of such fields, compared to the often-studied spherical Janus motors. By making use of analytical continuum theory and particle-based simulations we determine the concentration fields, and both the complex structure of the near-field and point-force dipole nature of the far-field behavior of the solvent velocity field that are important for studies of collective motor motion. We derive the dependence of motor velocity on geometric factors such as sphere size and dimer bond length and, thus, show how to construct motors with specific characteristics.

1 Introduction

Synthetic nanomotors that use chemical energy to produce directed motion are under active investigation because the autonomous motion of these motors can be exploited in new applications involving dynamics on very small scales. Starting with the first bimetallic rod nanomotors that move through self-electrophoresis as a result of an asymmetric distribution of catalytic activity[1,2], motors made from a variety of materials with various shapes and operating by different mechanisms were constructed.[3] Experiments demonstrated their potential uses as cargo transport vehicles and as elements in microfluidic devices, to name two of their many possible applications.[3–5]

The motion of an individual nanomotor and the interactions among many motors depend on the chemical gradients that arise from asymmetrical chemical activity and the fluid flows generated by motor motion. Both of these factors are integral parts of phoretic propulsion mechanisms and are strongly influenced by motor geometry. Janus motors with catalytic and noncatalytic faces have been studied extensively because these motors have a simple spherical geometry that facilitates theoretical modeling and fabrication.[6–10] For motors with more complex shapes it is important to understand how geometry influences motor motion and the dynamics of motor ensembles. In an effort to understand the role of geometry more thoroughly, we present a detailed study of a motor with a more complex but still analytically tractable chemical shape: a sphere-dimer motor where the catalytic and noncatalytic regions are confined to two linked spheres[11]. While such motors have been made and studied in the laboratory[12], their theoretical analysis is quite involved and the details of the propulsion mechanism differ from those of Janus motors.

Studies of small motors present challenges for theory since they operate out of equilibrium and often in the regime that lies on the borderline where macroscopic descriptions of their motion may break down. The macroscopic continuum theory for the self-diffusiophoretic motion of sphere-dimer motors is presented and tested against coarse-grained microscopic dynamics. The basis of the theoretical description has its antecedents in early work of Stimson and Jeffery[13], and more recent work of Popescu, Tasinkevych and Dietrich[14]. The theoretical description is generalized to treat spheres of arbitrary size with reactive boundary conditions that can account for both diffusion and reaction control. The characteristics of the flow field that arise in diffusiophoretic motion are computed. Our results show how various factors such as catalytic and noncatalytic sphere sizes, dimer bond length and reaction rates can be used to tune the motor velocity. The concentration and flow field results provide information that is needed to describe the nature of the propulsion of single motors as well as the collective interactions of many dimer motors.

2 Continuum Theory

Consider a sphere-dimer motor where a catalytic (S_1) sphere with radius r_1 is linked by a rigid bond of length d to a noncatalytic (S_2) sphere with radius r_2. The surrounding fluid is composed of A and B molecules and these species undergo

---

Chemical Physics Theory Group, Department of Chemistry, University of Toronto, Toronto, Ontario M5S 3H6, Canada. Email: sreigh@chem.utoronto.ca; rkapral@chem.utoronto.ca

the chemical reaction $A+S_1 \rightarrow B+S_1$ on the catalytic sphere with an intrinsic rate constant k_0. The chemical species interact with the catalytic and noncatalytic spheres in the dimer through intermolecular potentials, $U_{1,\alpha}$ and $U_{2,\beta}$ $(\alpha = A,B)$, respectively. We choose the interactions of A and B molecules with the S_1 sphere to be the same and those with the S_2 sphere to be different, but other choices are possible. For this choice the reaction at the S_1 sphere produces an inhomogeneous distribution of A and B species and the gradient of these species around the S_2 sphere is responsible for the propulsion of the motor. We assume that there is a large supply of the "fuel" A far from the motor so that concentration of A has the value $c_A = c_0$ far from the motor.

The sphere dimer is described in bispherical coordinates (θ,η,ϕ), $0 \le \theta \le \pi$, $-\infty \le \eta \le \infty$, and $0 \le \phi \le 2\pi$, shown in Fig. 1, which are related to the Cartesian coordinates (x,y,z) by the relations, $x = \xi \sin\theta \cos\phi/(\cosh\eta - \cos\theta)$, $y = \xi \sin\theta \sin\phi/(\cosh\eta - \cos\theta)$ and $z = \xi \sinh\eta/(\cosh\eta - \cos\theta)$, where ξ (>0) is a scale factor.[15,16] The S_1 and S_2 spheres are represented by the parameters $\eta = \eta_1 (>0)$ and $\eta = \eta_2 (<0)$, respectively. By choosing values of sphere radii of the S_1 and S_2 spheres, r_1 and r_2, and any separation distance, d, greater than the sum of their radii, the bispherical coordinate parameters, ξ, η_1 and η_2 are given by

$$\begin{aligned} \xi &= \frac{1}{2d}\sqrt{(d^2-r_1^2-r_2^2)^2-4r_1^2r_2^2}, \\ \eta_1 &= \ln\left(\xi/r_1+\sqrt{1+(\xi/r_1)^2}\right), \\ \eta_2 &= -\ln\left(\xi/r_2+\sqrt{1+(\xi/r_2)^2}\right). \end{aligned} \qquad (1)$$

Diffusiophoretic propulsion

The dimer velocity and the fluid flows associated with motor motion can be computed in the context of the diffusiophoretic mechanism.[14] In the continuum theory for diffusiophoretic self-propulsion[17–20], the self-generated concentration gradient gives rise to a fluid flow that results in a "slip" velocity at the outer edge of a boundary layer beyond which forces vanish. For the sphere dimer model we consider here, the catalytic reaction at the S_1 sphere is the source of this concentration gradient and its effect is felt at the noncatalytic S_2 sphere where the interaction potentials of the A and B species differ.

The c_A concentration field can be found by solving the steady-state diffusion equation, $\nabla^2 c_A = 0$, where the advection term is considered to be negligible. For the sphere dimer this equation must be solved subject to the boundary conditions,

$$\begin{aligned} (\boldsymbol{J}\cdot\hat{\boldsymbol{\eta}})_{\eta=\eta_1} &= \bar{k}_0 c_A(\eta=\eta_1), \\ (\boldsymbol{J}\cdot\hat{\boldsymbol{\eta}})_{\eta=\eta_2} &= 0, \end{aligned} \qquad (2)$$

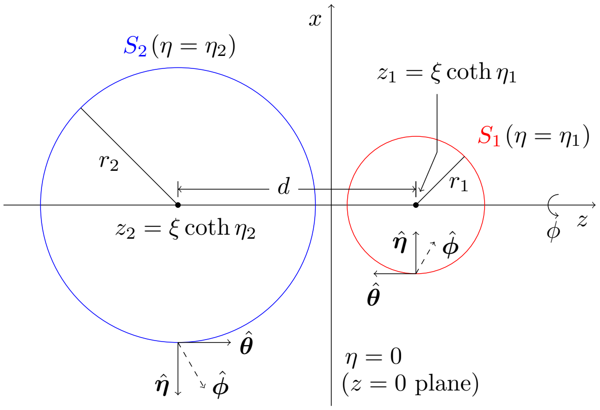

Fig. 1 Bispherical coordinate system (θ, η, ϕ) with the base unit vectors, $\hat{\boldsymbol{\theta}}$, $\hat{\boldsymbol{\eta}}$, $\hat{\boldsymbol{\phi}}$, for the sphere-dimer motor. The labels S_1 $(\eta=\eta_1)$ and S_2 $(\eta=\eta_2)$ represent the surfaces of the catalytic and noncatalytic spheres with radii r_1 (red) and r_2 (blue), respectively. The spheres with centers z_1 and z_2 are separated by a bond distance d.

at the catalytic and at noncatalytic spheres, respectively, where $\boldsymbol{J} = -D\nabla c_A$ is the flux of the A concentration field, $\bar{k}_0 = k_0/(4\pi r_1^2)$, and D is the common diffusion constant of the A and B species. The direction of $\hat{\boldsymbol{\eta}}$ is the normal to the surface of the spheres. The c_B field can be found from the conservation condition, $c_A + c_B = c_0$, and is given by[15]

$$\begin{aligned} c_B(\theta,\eta) = &-\sqrt{\cosh\eta-\mu} \\ &\times \sum_{l=0}^{\infty}[A_l e^{(l+\frac{1}{2})\eta} + B_l e^{-(l+\frac{1}{2})\eta}]P_l(\mu), \end{aligned} \qquad (3)$$

where $P_l(\mu)$ is a Legendre function and $\mu = \cos\theta$. The A_l and B_l coefficients can be determined from the boundary conditions by solving a set linear matrix equations (see Appendix).

Given this concentration field, the slip velocity of the fluid at the outer edge of a boundary layer can be written as $\boldsymbol{v}_s = -\kappa\nabla_\theta c_B$,[18,19] where $\kappa = (k_BT/\bar{\mu})\Lambda$ and

$$\Lambda = \int_0^\infty r[e^{-U_{2,B}(r)/(k_BT)} - e^{-U_{2,A}(r)/(k_BT)}]dr, \qquad (4)$$

with $\bar{\mu}$ the shear viscosity, k_B the Boltzmann constant, and T the temperature. The fluid flow field outside of the interfacial region is governed by the Stokes equation, $\nabla p = \bar{\mu}\nabla^2\boldsymbol{v}$, with the incompressibility condition, $\nabla\cdot\boldsymbol{v} = 0$, where p is the pressure and $\boldsymbol{v}$ is the fluid velocity field. The fluid velocity may be expressed in terms of Stokes' stream function ψ from $\boldsymbol{v} = \hat{\boldsymbol{\phi}}/\rho \times \nabla\psi$[16], where $\rho = \xi\sin\theta/(\cosh\eta-\mu)$. The stream function satisfies $E^4(\psi) = 0$, where $E^4 = E^2(E^2)$ and $E^2 = (\cosh\eta-\mu)/\xi^2[\partial/\partial\eta\{(\cosh\eta-\mu)\partial/\partial\eta\} + (1-\mu^2)\partial/\partial\mu\{(\cosh\eta-\mu)\partial/\partial\mu\}]$.[13,16]

In the laboratory frame where the motor moves with velocity V, the boundary conditions at the outer edges of interfacial regions around the S_1 and S_2 spheres are given by

$$\begin{aligned}(\psi+\tfrac{1}{2}\rho^2 V)|_{\eta=\eta_1,\eta_2} &= 0,\\ \partial/\partial\eta(\psi+\tfrac{1}{2}\rho^2 V)|_{\eta=\eta_1} &= 0,\\ \partial/\partial\eta(\psi+\tfrac{1}{2}\rho^2 V)|_{\eta=\eta_2} &= \kappa\rho\partial c_B/\partial\theta|_{\eta=\eta_2}.\end{aligned} \tag{5}$$

The stream function equation can be exactly solved and the solution is[13]

$$\psi=(\cosh\eta-\mu)^{-\frac{3}{2}}\sum_{l=1}^{\infty}W_l(\eta)V_l(\mu), \tag{6}$$

where $W_l(\eta)=a_l\cosh(l-\frac{1}{2})\eta+b_l\sinh(l-\frac{1}{2})\eta+c_l\cosh(l+\frac{3}{2})\eta+d_l\sinh(l+\frac{3}{2})\eta$ and $V_l(\mu)=P_{l-1}(\mu)-P_{l+1}(\mu)$. The coefficients a_l, b_l, c_l, and d_l are determined by the boundary conditions (see Appendix).

Since no external forces act on the system and the sphere-solvent forces are zero outside the interfacial zone, we have

$$F_z=\int_{S_1}\mathbf{\Pi}_z\cdot\hat{\boldsymbol{n}}dS+\int_{S_2}\mathbf{\Pi}_z\cdot\hat{\boldsymbol{n}}dS=0, \tag{7}$$

where $\mathbf{\Pi}$ is the stress tensor, $\mathbf{\Pi}_z=\hat{\boldsymbol{z}}\cdot\mathbf{\Pi}$, $\hat{\boldsymbol{n}}$ is the surface normal vector and the surface integrals are taken at the outer edge of the interfacial zone. The system is symmetric around the azimuthal angle ϕ and only the force in the z-direction needs to be considered. The velocity of sphere dimer follows from this condition and is

$$V=\xi\kappa\frac{\sum_{l=1}^{\infty}(2l+1)\Phi_l\Xi_l/\Delta_l}{\sum_{l=1}^{\infty}(2l+1)f_l(\bar{a}_l+\bar{c}_l)/\Delta_l}, \tag{8}$$

where the coefficients in this equation are given in the Appendix.

3 Microscopic dynamics

In the microscopic model the fluid (solvent) comprising A and B species is represented by N_s particles of mass m with positions $\boldsymbol{r}_i(t)$ and velocities $\boldsymbol{v}_i(t)$, where $i=1,\ldots,N_s$. We consider a single sphere-dimer motor. The spheres in the dimer motor interact with the A and B molecules through repulsive Lennard-Jones (LJ) potentials, $U=4\varepsilon[(\sigma/r)^{12}-(\sigma/r)^6]+\varepsilon$ for $r<2^{1/6}\sigma$ and $U=0$ for $r\geq 2^{1/6}\sigma$, with energy ε and distance σ parameters. As noted earlier, we choose the interaction energies of A and B molecules with the S_1 sphere to be the same ($\varepsilon_A=\varepsilon_B=\varepsilon$) and those with the S_2 sphere to be different ($\varepsilon_B<\varepsilon_A=\varepsilon$). For $\varepsilon_B<\varepsilon_A$ the dimer motor moves with the S_1 sphere at its head. An irreversible chemical reaction $A\rightarrow B$ occurs at the catalytic sphere S_1 whenever A encounters S_1. Collisions of A or B molecules with the noncatalytic sphere S_2 do not lead to reactions. To maintain a large supply of the “fuel” A far from the motor, B is converted to A at a distance d_p.

The dynamics of this system is simulated using a hybrid method that combines molecular dynamics (MD) for sphere dimers and multiparticle collision (MPC) dynamics for the fluid particles.[21] In this method there are no explicit intermolecular potentials among the solvent particles; these interactions are accounted for by multiparticle collisions. The dynamics consists of alternating streaming and collision steps. In the streaming step, the particles move by Newton’s equations of motion. At time intervals h, called the collision time, the solvent particles are sorted into cubic cells of side length a and their relative velocities, with respect to the center-of-mass velocities of each cell, are rotated around a randomly oriented axis by a fixed angle α. The particle velocity after collision is given by $\boldsymbol{v}_i(t+h)=\boldsymbol{v}_{cm}(t)+\mathscr{R}(\alpha)(\boldsymbol{v}_i(t)-\boldsymbol{v}_{cm}(t))$, where $\mathscr{R}(\alpha)$ is the rotation matrix and $\boldsymbol{v}_{cm}=\Sigma_{j=1}^{N_c}\boldsymbol{v}_j/N_c$ is the center-of-mass velocity of the particles in the cell to which the particle i belongs, and N_c is the number of particles in that cell. A random shift of the collision lattice is applied at every collision step to ensure Galilean invariance.[22]

All quantities are reported in dimensionless units where length, energy, mass and time are measured in units of the MPC cell length $a=\sigma$, ε, the solvent mass m, and $\sigma\sqrt{m/\varepsilon}$, respectively. Multiparticle collisions are carried out by dividing the cubic simulation box with linear dimension L into $L^3=60^3-120^3$ cubic cells and performing velocity rotations by an angle $\alpha=130^\circ$ about randomly chosen axes at time intervals of $h=0.1$ for the MPC collision steps. The average solvent number density is $c_0=10$ and the temperature is $k_BT=1$. The MD time step is $\Delta t=0.01$. The parameters in the S_2 sphere-solvent repulsive LJ potentials are $\varepsilon_A=1.0$ and $\varepsilon_B=0.1$ for A and B, respectively, while $\varepsilon_A=\varepsilon_B=1.0$ for the S_1 sphere. The σ_i ($i=1,2$) values fix the sizes of the S_1 and S_2 spheres. The sphere mass is $M_i=4\pi(2^{1/6}\sigma_i)^3c_0/3$ ($i=1,2$). The transport properties of the fluid depend on h, α, and N_c. and these parameters were chosen to model fluids with a high Schmidt number S_c and low Reynolds number R_e. The fluid viscosity is $\bar{\mu}=mN_c\nu=8.7$, where ν is the kinematic viscosity, the diffusion constant is given by $D=0.0514$ and the Schmidt number is $S_c=\nu/D=17$, which ensures that momentum transport dominates over mass transport. In addition, the small value of the Péclet number, $Pe=Va/D<1$, implies that diffusion is dominant over advection.

4 Comparison of continuum and microscopic dynamics

The continuum c_B concentration field is shown in Fig. 2(a) in the xz-plane. It is not spherically symmetrical around the

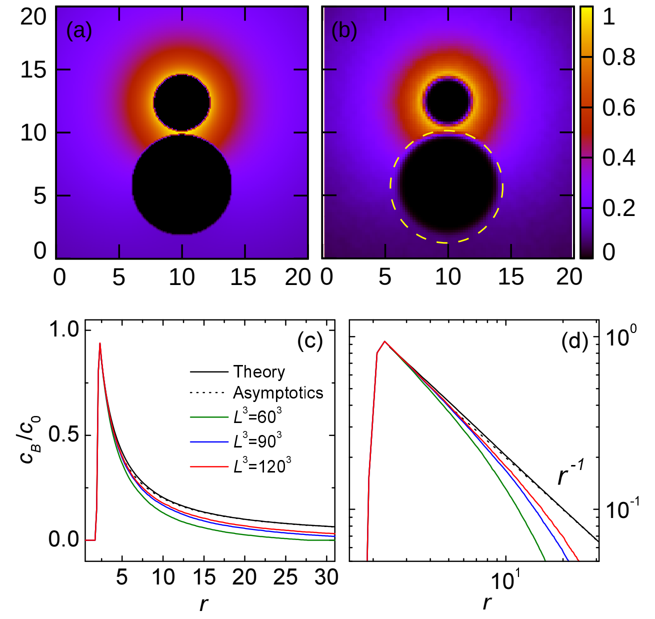

Fig. 2 Normalized (c_B/c_0) c_B field in the xz plane $(y=0)$ from (a) the continuum theory and (b) MD-MPCD simulations; dashed circle indicates where the potential goes to zero. (c) Plot of c_B versus r in the $\vartheta = 90°$ plane in the spherical polar coordinate (r, ϑ, ϕ) from the center of S_1; continuum theory (black solid line), its asymptote (dotted lines); and simulation results for different system sizes: $L = 60$ $(d_p = 28)$ (green line), $L = 90$ $(d_p = 43)$ (blue line), and $L = 120$ $(d_p = 58)$ (red line) . (d) Log-log plot showing the asymptotic decay of c_B. Color coding same as in (c).

catalytic sphere, and gives rise to the concentration gradient around the noncatalytic sphere which is responsible for propulsion. Figures 2(c) and (d) shows the c_B field in more quantitative detail in a specific region of the $\vartheta = 90°$ plane with respect to the catalytic sphere, where $\vartheta = \cos^{-1}(z/r)$ is the polar angle in spherical polar coordinates, (r, ϑ, ϕ); $x = r \sin\vartheta \cos\phi$, $y = r \sin\vartheta \sin\phi$, and $z = r\cos\vartheta$. It decays with distance and for large r one has $c_B \sim -\sqrt{2}\xi \sum_{l=1}^{\infty}(A_l + B_l)/r + \mathscr{O}(1/r^2)$, with a r^{-1} decay as expected for the solution of a diffusion equation.

The simulated c_B field is shown in Fig. 2(b) (cf. Fig. 2(a)) and compared with the continuum theory in panel (c). One can see that theory and simulation agree very well, but there are discrepancies at distances far from the dimer that can be ascribed to finite-size effects. From Figs. 2(c) and (d) one observes that as the system size increases, the simulation results approach the theoretical curve.

The sphere sizes, fluid transport coefficients and boundary condition parameters that enter the theoretical formulas must be specified to make such comparisons. The results in the figure are for a dimer with $\sigma_1 = 2$ and $\sigma_2 = 4$ and bond length $d = 6.5$, and these values were used as radii and bond distance in the theoretical equations. Due to the soft nature of the repulsive LJ potentials there is some ambiguity, of the order of the boundary layer thickness, in the precise choice of radius. The intrinsic reaction rate constant can be estimated from simple collision theory as $\bar{k}_0 \sim \sqrt{k_BT/2\pi m} \sim 0.4$, and this approximate value was used in the boundary condition.

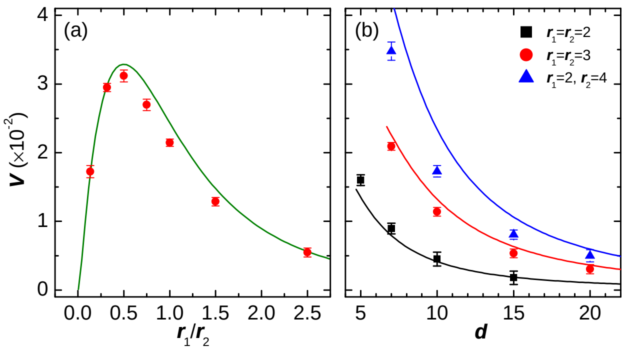

Fig. 3 (a) Plot of V versus r_1/r_2 for $r_2 = \sigma_2 = 3$: continuum theory (solid line), simulation (bullets). (b) Plot of V versus d for several different dimers: continuum theory (solid lines), simulation (symbols). The parameter values are given in the text.

Figure 3 plots the motor velocity V for various sphere sizes and bond distances $d = r_1 + r_2 + \Delta$. Experiments and earlier simulations suggested that V exhibits a maximum as r_1 (catalytic sphere) increases for fixed r_2 and Δ.[12] Panel (a) shows that the continuum theory predicts such a maximum and also provides the shape of the curve for the entire range of radius values. The extensive MPC simulation results are in good agreement with the theoretical results. By contrast, for fixed r_1 one finds that V increases approximately logarithmically with increasing r_2. The theory is also able to describe the variation of V with d for fixed r_1 and r_2[14], including the d^{-2} decay at large distances (see Fig. 3(b)); however, there are small discrepancies in the absolute magnitude of the velocity, especially for motors with spheres of unequal size. The continuum theory does not fully describe microscopic details within the boundary layer and the boundary conditions involve input parameters that can be specified only approximately. Nor does it account for the presence of thermal fluctuations. Nevertheless, the general trends of the variations of V with d are captured by the continuum theory.

5 Fluid Flow Fields

The streamlines describing fluid motion may be constructed from the stream function by setting ψ = constant. The fluid velocity may also computed from the stream functions using $\boldsymbol{v} = \hat{\boldsymbol{\phi}}/\rho \times \nabla\psi$.

Figure 4 shows the fluid streamlines and velocity fields near to and far from the dimer. In the near-field, one sees a complex

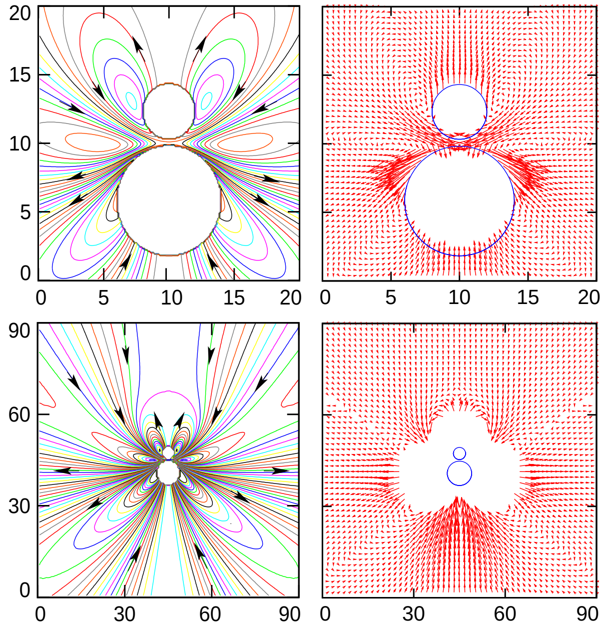

Fig. 4 Fluid streamlines for a dimer motor with the radii, $r_1 = 2$, $r_2 = 4$, and the bond length $d = 6.5$ are shown in the near field (upper left) and in the far field (lower left) for $\varepsilon_B < \varepsilon_A$. The corresponding velocity fields are shown in the near field (upper right) and in the far field (lower right).

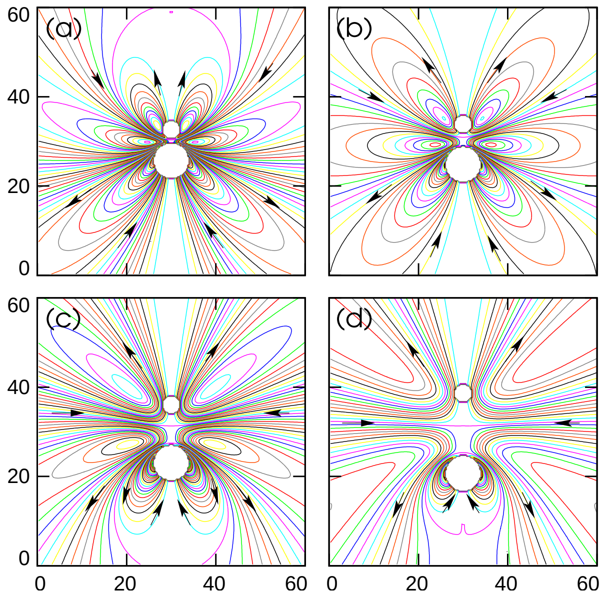

Fig. 5 Fluid streamlines for the various dimer bond lengths: (a) $d = 7$, (b) $d = 9$, (c) $d = 13$, and (d) $d = 18$.

fluid flow field with several vortices. Fluid is pushed from the front of the catalytic sphere and, as a result of local circulation, it returns to the rear of this sphere. This influx of fluid is strongly expelled in a direction tangential to the noncatalytic sphere, and then again returns to the rear of the sphere. This picture of the near-field fluid flow was partially captured in earlier simulations.[23–25]. The far-field flow is more difficult to obtain from simulations because of finite-size limitations. Our analytical results show that fluid flows toward the sphere dimer from both the front and back, and moves away from the dimer in the lateral directions, a pattern characteristic of a point-force-dipolar flow field, $-fd_0(3\cos^2\vartheta - 1)\hat{\boldsymbol{r}}/(8\pi\bar{\mu}r^2)$, where f is the magnitude of force, d_0 is the separation between the point forces, and r is the distance from the force dipole. (See also Hernandez-Ortiz, et al.[26])

Figure 5 shows the fluid streamlines for various motor bond lengths. When the bond length is small ($d \lesssim 9$), the streamlines and the velocity field are similar to those discussed in Fig. 4. As the bond length increases, the circulation of fluid with a stagnation region in front of the catalytic sphere (seen in the panel (a)) retreats from the catalytic sphere. For a bond length $d \sim 9$ (Fig. 5 (b)), the streamlines have a symmetric form with several local circulation regions and no stagnation region. As the bond length increases to even larger values ($d \gtrsim 9$) (Fig. 5 (c)), a stagnation region appears in the vicinity of the noncatalytic sphere. Fluid enters in the lateral directions and is pushed to the frontward and backward directions as a result of local circulation. When the bond length increases further ($d \sim 13$) (Fig. 5 (d)), the dimer motor behaves approximately as two independent spheres subject to external forces. The fluid field around the catalytic sphere displays a pattern characteristic of sedimentation, and the fluid flow around the noncatalytic sphere shows a dipolar field pattern similar to a spherical Janus motor.

Figure 6 plots the magnitude of the fluid velocity versus distance from the dimer. If $\boldsymbol{v}$ is written in the form $\boldsymbol{v} = v_\theta\hat{\boldsymbol{\theta}} + v_\eta\hat{\boldsymbol{\eta}}$, and its components are expanded in terms of the distance r from the origin, then, from the force-free condition, we obtain the asymptotic expressions: $v_\theta = -\sqrt{2}\sin\vartheta(1-3\cos^2\vartheta)\Omega/r^2 + \mathscr{O}(1/r^3)$ and $v_\eta = 2\sqrt{2}\cos\vartheta(1-\frac{3}{2}\sin^2\vartheta)\Omega/r^2 + \mathscr{O}(1/r^3)$, where $\Omega = \sum_{l=1}^{\infty}(2l+1)\{(l-1/2)b_l + (l+3/2)d_l\}$. Thus, $\boldsymbol{v}$ decays as r^{-2}, consistent with recent simulations.[25] Two representative examples of the variation of the magnitude of the fluid velocity with r for small ($d = 6.8$) and large ($d = 13$) bond lengths are shown in Fig. 6 (a) and (b). A stagnation region (sharp dip in curve) appears only in front of the catalytic sphere ($\vartheta = 0°$) for the small bond length dimer ($d = 6.8$) (Fig. 6 (a) and see also Fig. 5 (a)) and only behind the noncatalytic sphere ($\vartheta = 180°$) for the large bond length dimer ($d = 13$) (Fig. 6 (b) and also Fig. 5 (c)). When the bond length is smaller than a certain critical length ($d \sim 9$), the stagnation point moves to larger r as the bond distance increases (Fig. 6 (c)). However, when the bond length is larger than this critical value, the stagnation

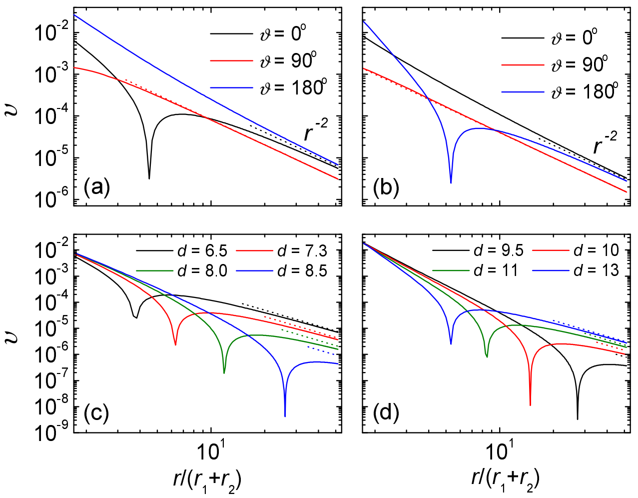

Fig. 6 Plots of the magnitude of the fluid velocity, $v = \sqrt{v_\theta^2 + v_\eta^2}$, for dimers with bond lengths (a) $d = 6.8$ and (b) $d = 13$, in the forward (black, $\vartheta = 0^\circ$), backward (blue, $\vartheta = 180^\circ$), and side (red, $\vartheta = 90^\circ$) directions as a function of distance r from the origin (ϑ is the polar angle in the spherical polar coordinate system); (dotted lines) asymptotic limits (see text). A stagnation region is seen due to the fluid circulation shown in Fig. 5. The magnitude of fluid velocity versus r for dimers with different bond lengths are shown in (c) $\vartheta = 0^\circ$ directions and (d) $\vartheta = 180^\circ$ directions.

point moves to smaller r as the bond length increases (Fig. 6 (d)).

6 Propulsion force

In the diffusiophoretic mechanism the self-generated concentration gradient that arises from the asymmetrical motor catalytic activity leads to a body force on the motor. Since the entire system is force-free, momentum conservation requires that fluid flows are generated in the system, and these flows are an integral part of the propulsion mechanism. Our detailed calculations have shown how the motor velocity can be determined from this picture of the dynamics. The forces that the motor experiences are very different from those that give rise to Stokes law friction coefficients when a colloidal particle is subject to an external force.

The body force on the motor is a well-defined mechanical quantity that is determined by the intermolecular interactions of the solvent species with the motor, and it depends on the fuel and product concentration fields in the vicinity of the motor. It is ultimately this force that is the origin of the propulsion. Through total momentum conservation this force is opposite to the total force on the solvent. If $U(\mathbf{r}^N)$ is the total potential energy, the body force exerted on the motor by interactions with the fluid is $\mathbf{F} = \sum_{i=1}^{N} \partial U/\partial \mathbf{r}_i$ where $\mathbf{r}_i$ is the position of fluid particle i. Momentum conservation was used to express this force in terms of derivatives with respect to solvent coordinates. The steady state average value of this force projected along the propagation direction, F_p, is defined to be the propulsion force.

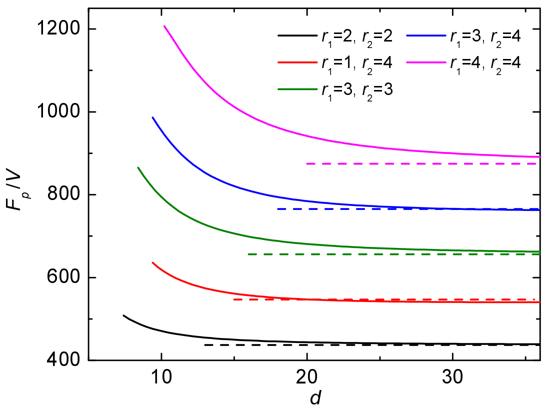

Fig. 7 Plots of the ratio (F_p/V) versus bond length d for dimer motors with the various radii. The solid lines are analytic calculations and the dashed lines indicate $4\pi\bar{\mu}(r_1+r_2)$. The black, red, green, blue, magenta lines correspond to radii (r_1,r_2) = (2,2), (1,4), (3,3), (3,4), (4,4), respectively.

We first consider a spherical Janus particle where catalytic reactions on one side of the particle convert fuel A to product B, $A \to B$. The A and B species interact with the Janus particle through central intermolecular potentials $U_{J,A}$ and $U_{J,B}$. The diffusiophoretic velocity along the propagation direction of the motor, $\hat{\mathbf{z}}$, can be determined from the surface average, $\langle \dots \rangle_{\mathscr{S}}$, of the slip velocity, $V = -\langle \hat{\mathbf{z}} \cdot \mathbf{v}_s \rangle_{\mathscr{S}}$, where the slip velocity at the outer edge of the boundary layer surrounding the Janus particle is given by $\mathbf{v}_s = -(k_BT/\bar{\mu})\Lambda_J \nabla_\theta c_B(r_J,\vartheta)$, with Λ_J defined by

$$\Lambda_J = \int_0^\infty r[e^{-U_{J,B}(r)/(k_BT)} - e^{-U_{J,A}(r)/(k_BT)}]dr. \qquad (9)$$

The surface average of the slip velocity can be re-expressed using integration by parts to give,

$$V = \frac{k_BT}{\bar{\mu} r_J}\Lambda_J \int_{-1}^{1} d\mu\, \mu c_B(r_J,\mu), \qquad (10)$$

where μ is now given by $\mu = \cos\vartheta$ in the spherical polar coordinate system. The Janus particle propulsion force can be written a similar form,

$$F_p = 4\pi k_BT\Lambda_J \int_{-1}^{1} d\mu\, \mu c_B(r_J,\mu). \qquad (11)$$

Since both the average velocity and propulsion force for the Janus particle are known, we may use the ratio, $\zeta_J = F_p/V$, which is simply another expression for total momentum conservation, to define an effective friction coefficient, ζ_J. Using the above equations, this ratio, $F_p/V = 4\pi\bar{\mu}r_J$, is 2/3 of the stick Stokes friction, $\zeta_S = 6\pi\bar{\mu}r_J$. As expected, the effective friction coefficient defined in this way is not equal to the friction coefficient for the particle subject to an external force.

The propulsion force for the sphere dimer may be computed explicitly [11] and its value depends on the intermolecular potentials and steady state concentration fields. It may be written as

$$F_p = 4\pi k_B T \Lambda \int_{-1}^{1} d\mu \; \mu c_B(\mu,\eta_2), \tag{12}$$

where $\mu = \cos\theta$ in bispherical coordinates. Since the average velocity of the dimer is known (the expression for this quantity was given in Eq. (8)), we may use the ratio, $\zeta(r_1,r_2,d) = F_p/V$, to define an effective friction coefficient for the dimer motor. This ratio, which now also depends on the dimer bond length as well as the sphere radii, is plotted versus d in Fig. 7 for various values of r_1 and r_2. For large bond lengths, $\zeta(r_1,r_2,d)$ becomes independent of d and approaches $\zeta = \zeta_1 + \zeta_2$, the sum of individual friction coefficients of the two spheres, where $\zeta_i = 4\pi\bar{\mu}r_i$. As the bond length d decreases, $\zeta(r_1,r_2,d)$ increases sharply, and this reflects the change in character of the fluid flow fields as the dimer bond length changes, which was discussed in the previous section.

7 Conclusions

Motor geometry can strongly affect motor velocity, concentration gradients and hydrodynamics flow fields. In particular, we have shown how changes in the sphere sizes and dimer bond length can influence the magnitude of the motor velocity. The force dipolar flow field and r^{-2} power law decay for dimer motors with small bond lengths resemble those of microorganisms such as *C. reinhardtii* (puller) that can also be described as a point-force-dipole and exhibit the same power law decay.[27] Also, when $\varepsilon_B > \varepsilon_A$, the sphere dimer will reverse direction and the flow field will be characteristic of a pusher, similar to that of *E. coli*.[28] Thus, sphere dimers exhibit far-field hydrodynamic effects similar to those of biological swimmers and different from the r^{-3} decay of spherical Janus motors. Moreover, it is notable that the far-field flow pattern reverses as the bond length changes. For small bond lengths, the far-field flow pattern is characteristic of a puller as noted above, but it changes to a pattern characteristic of a pusher for large dimer bond lengths. Consequently, depending on its bond length, a dimer motor can exhibit flow patterns that are similar to those of pusher or puller biological swimmers. More generally, we have seen that the short and long range structures of the c_B and $\boldsymbol{v}$ fields are very different and this, in turn, will lead to phenomena that depend in non-trivial ways on the concentration of motors when the collective behavior of sphere-dimer and other complex motors is studied.[29–32]

Acknowledgments: This work was supported in part by a grant from the Natural Sciences and Engineering Council of Canada. A portion of the computational work was performed at the SciNet, which is funded by the Canada Foundation for Innovation under the auspices of Compute Canada, the Government of Ontario, Ontario Research Fund-Research Excellence, and the University of Toronto.

8 Appendix: Derivation of solutions

8.1 Concentration distribution

The steady-state c_A field around the sphere dimer satisfies the diffusion equation, $\nabla^2 c_A = 0$, subject to the radiation and reflecting boundary conditions for the S_1 and S_2 spheres given in Eqs. (2). The general solution of the c_A concentration field can be expressed in the form given in Eq. (3) using $c_A + c_B = c_0$.

The coefficients A_l and B_l in this equation can be determined as follows: The boundary conditions, Eq. (2), can be rewritten in terms of the Legendre functions using the formula,[15]

$$\frac{1}{\sqrt{\cosh\eta - \mu}} = \sqrt{2}\sum_{l=0}^{\infty} e^{-(l+\frac{1}{2})|\eta|} P_l(\mu), \tag{13}$$

and the recurrence relation,[33]

$$(2l+1)\mu P_l = (l+1)P_{l+1} + lP_{l-1}. \tag{14}$$

We obtain the following equality for the l^{th} term ($l \geqslant 1$) in Legendre series from the radiation boundary condition in Eq. (2),

$$\begin{aligned}
&-le^{(l-\frac{1}{2})\eta_1}A_{l-1} + le^{-(l-\frac{1}{2})\eta_1}B_{l-1} \\
&+[\{\sinh\eta_1 + (2l+1)\cosh\eta_1\} + 2\xi\bar{k}_0/D]e^{(l+\frac{1}{2})\eta_1}A_l \\
&+[\{\sinh\eta_1 - (2l+1)\cosh\eta_1\} + 2\xi\bar{k}_0/D]e^{-(l+\frac{1}{2})\eta_1}B_l \\
&-(l+1)e^{(l+\frac{3}{2})\eta_1}A_{l+1} + (l+1)e^{-(l+\frac{3}{2})\eta_1}B_{l+1} \\
&= -\frac{2\sqrt{2}\xi\bar{k}_0}{D}C_0 e^{-(l+\frac{1}{2})\eta_1}.
\end{aligned} \tag{15}$$

From the reflecting boundary condition in Eq. (2), we obtain

$$\begin{aligned}
&-le^{(l-\frac{1}{2})\eta_2}A_{l-1} + le^{-(l-\frac{1}{2})\eta_2}B_{l-1} \\
&+[\sinh\eta_2 + (2l+1)\cosh\eta_2]e^{(l+\frac{1}{2})\eta_2}A_l \\
&+[\sinh\eta_2 - (2l+1)\cosh\eta_2]e^{-(l+\frac{1}{2})\eta_2}B_l \\
&-(l+1)e^{(l+\frac{3}{2})\eta_2}A_{l+1} + (l+1)e^{-(l+\frac{3}{2})\eta_2}B_{l+1} = 0.
\end{aligned} \tag{16}$$

In Eqs. (15) and (16), the coefficients A_l and B_l may be solved by writing the equations as infinite matrix formulas,[34]

$$\begin{aligned}
\mathbb{M}\boldsymbol{A} + \mathbb{N}\boldsymbol{B} &= \boldsymbol{E}, \\
\mathbb{O}\boldsymbol{A} + \mathbb{P}\boldsymbol{B} &= \boldsymbol{O},
\end{aligned} \tag{17}$$

Table 1 The elements of matrices and vectors in Eq. (17) ($l \geqslant 1$).

$$
\begin{aligned}
&\mathbb{M}_{l,l} = \{\sinh\eta_1 + (2l-1)\cosh\eta_1\}e^{(l-\frac{1}{2})\eta_1} + \frac{2\xi\bar{k}_0}{D}e^{(l-\frac{1}{2})\eta_1},\\
&\mathbb{M}_{l+1,l} = -le^{(l-\frac{1}{2})\eta_1},\\
&\mathbb{M}_{l,l+1} = -le^{(l+\frac{1}{2})\eta_1},\\
&\mathbb{N}_{l,l} = \{\sinh\eta_1 - (2l-1)\cosh\eta_1\}e^{-(l-\frac{1}{2})\eta_1} + \frac{2\xi\bar{k}_0}{D}e^{-(l-\frac{1}{2})\eta_1},\\
&\mathbb{N}_{l+1,l} = le^{-(l-\frac{1}{2})\eta_1},\\
&\mathbb{N}_{l,l+1} = le^{-(l+\frac{1}{2})\eta_1},\\
&\mathbb{O}_{l,l} = \{\sinh\eta_2 + (2l-1)\cosh\eta_2\}e^{(l-\frac{1}{2})\eta_2},\\
&\mathbb{O}_{l+1,l} = -le^{(l-\frac{1}{2})\eta_2},\\
&\mathbb{O}_{l,l+1} = -le^{(l+\frac{1}{2})\eta_2},\\
&\mathbb{P}_{l,l} = \{\sinh\eta_2 - (2l-1)\cosh\eta_2\}e^{-(l-\frac{1}{2})\eta_2},\\
&\mathbb{P}_{l+1,l} = le^{-(l-\frac{1}{2})\eta_2},\\
&\mathbb{P}_{l,l+1} = le^{-(l+\frac{1}{2})\eta_2},\\
&\boldsymbol{A}_l = A_{l-1},\\
&\boldsymbol{B}_l = B_{l-1},\\
&\boldsymbol{E}_l = -\frac{2\sqrt{2}\xi\bar{k}_0C_0}{D}e^{-(l-\frac{1}{2})\eta_1},\\
&\boldsymbol{O}_l = 0.
\end{aligned}
$$

where $\mathbb{M}$, $\mathbb{N}$, $\mathbb{O}$ and $\mathbb{P}$ are the tridiagonal infinite matrices and $\boldsymbol{A}$, $\boldsymbol{B}$, $\boldsymbol{E}$, and $\boldsymbol{O}$ are the infinite column vectors. The elements of these matrices and vectors are given in Table 1. By formally inverting the matrices, the vectors $\boldsymbol{A}$ and $\boldsymbol{B}$ are found to be

$$
\begin{aligned}
\boldsymbol{A} &= [\mathbb{M} - \mathbb{N}\mathbb{P}^{-1}\mathbb{O}]^{-1}\boldsymbol{E},\\
\boldsymbol{B} &= -\mathbb{P}^{-1}\mathbb{O}[\mathbb{M} - \mathbb{N}\mathbb{P}^{-1}\mathbb{O}]^{-1}\boldsymbol{E}.
\end{aligned}
\tag{18}
$$

8.2 Propulsion velocity

If we define $\chi = \sum_{l=1}^{\infty} W_l(\eta)V_l(\mu)$, the boundary conditions in Eq. (5) are given by

$$
\begin{aligned}
\chi|_{\eta=\eta_1,\eta_2} &= -\frac{\xi^2V(1-\mu^2)}{2(\cosh\eta-\mu)^{1/2}}\bigg|_{\eta=\eta_1,\eta_2},\\
\frac{\partial\chi}{\partial\eta}\bigg|_{\eta=\eta_1} &= \frac{\xi^2V(1-\mu^2)\sinh\eta}{4(\cosh\eta-\mu)^{3/2}}\bigg|_{\eta=\eta_1},\\
\frac{\partial\chi}{\partial\eta}\bigg|_{\eta=\eta_2} &= \frac{\xi^2V(1-\mu^2)\sinh\eta}{4(\cosh\eta-\mu)^{3/2}}\bigg|_{\eta=\eta_2} + \xi\kappa\sum_{l=0}^{\infty}\Big[A_le^{(l+\frac{1}{2})\eta}\\
&\quad + B_le^{-(l+\frac{1}{2})\eta}\Big]\bigg[-\frac{(1-\mu^2)P_l}{2}\\
&\quad + (\cosh\eta-\mu)(1-\mu^2)\frac{\partial P_l}{\partial\mu}\bigg]\bigg|_{\eta=\eta_2}.
\end{aligned}
\tag{19}
$$

Using the relations, [13,33]

$$
\begin{aligned}
(1-\mu^2)P_l &= \frac{(l+1)(l+2)}{(2l+1)(2l+3)}V_{l+1} - \frac{l(l-1)}{(2l+1)(2l-1)}V_{l-1},\\
(1-\mu^2)\frac{dP_l}{d\mu} &= \frac{l(l+1)}{(2l+1)}V_l,\\
\mu V_l &= \frac{l-1}{2l-1}V_{l-1} + \frac{l+2}{2l+3}V_{l+1},
\end{aligned}
\tag{20}
$$

and Eq. (13), we may expand the right hand sides of Eq. (19) in a series of V_l as

$$
\chi = -\frac{\xi^2V}{\sqrt{2}}\sum_{l=1}^{\infty}\frac{l(l+1)}{2l+1}\left[\frac{e^{\mp(l-\frac{1}{2})\eta}}{2l-1} - \frac{e^{\mp(l+\frac{3}{2})\eta}}{2l+3}\right]V_l, \tag{21}
$$

for $\eta = \eta_1, \eta_2$ and

$$
\frac{\partial\chi}{\partial\eta} = \pm\frac{\xi^2V}{2\sqrt{2}}\sum_{l=1}^{\infty}\frac{l(l+1)}{2l+1}[e^{\mp(l-\frac{1}{2})\eta} - e^{\mp(l+\frac{3}{2})\eta}]V_l + \Gamma, \tag{22}
$$

where $\Gamma = 0$ for $\eta = \eta_1$ and $\Gamma = \xi\kappa\sum_{l=1}^{\infty}\Phi_lV_l$ for $\eta = \eta_2$. The upper sign and lower sign are taken for $\eta = \eta_1$ and $\eta = \eta_2$, respectively. Since both sides of Eqs. (21) and (22) are expanded in a series of V_l, we can determine the unknown coefficients of $W_l(\eta)$ in Eq. (6) from the following equations:

$$\begin{aligned}
&a_l \cosh(l-\tfrac{1}{2})\eta_1 + b_l \sinh(l-\tfrac{1}{2})\eta_1 \\
&\quad + c_l \cosh(l+\tfrac{3}{2})\eta_1 + d_l \sinh(l+\tfrac{3}{2})\eta_1 \\
&\qquad = -\gamma_l\{(2l+3)e^{-(l-\frac{1}{2})\eta_1} - (2l-1)e^{-(l+\frac{3}{2})\eta_1}\}, \\
&a_l \cosh(l-\tfrac{1}{2})\eta_2 + b_l \sinh(l-\tfrac{1}{2})\eta_2 \\
&\quad + c_l \cosh(l+\tfrac{3}{2})\eta_2 + d_l \sinh(l+\tfrac{3}{2})\eta_2 \\
&\qquad = -\gamma_l\{(2l+3)e^{(l-\frac{1}{2})\eta_2} - (2l-1)e^{(l+\frac{3}{2})\eta_2}\}, \\
&(2l-1)\{a_l \sinh(l-\tfrac{1}{2})\eta_1 + b_l \cosh(l-\tfrac{1}{2})\eta_1\} \\
&\quad + (2l+3)\{c_l \sinh(l+\tfrac{3}{2})\eta_1 + d_l \cosh(l+\tfrac{3}{2})\eta_1\} \\
&\qquad = (2l-1)(2l+3)\gamma_l\{e^{-(l-\frac{1}{2})\eta_1} - e^{-(l+\frac{3}{2})\eta_1}\}, \\
&(2l-1)\{a_l \sinh(l-\tfrac{1}{2})\eta_2 + b_l \cosh(l-\tfrac{1}{2})\eta_2\} \\
&\quad + (2l+3)\{c_l \sinh(l+\tfrac{3}{2})\eta_2 + d_l \cosh(l+\tfrac{3}{2})\eta_2\} \\
&\qquad = -(2l-1)(2l+3)\gamma_l\{e^{(l-\frac{1}{2})\eta_2} - e^{(l+\frac{3}{2})\eta_2}\} \\
&\qquad + 2\xi\kappa\Phi_l,
\end{aligned} \tag{23}$$

where $\gamma_l = f_l V$. The solution of the above equations for the unknown coefficients a_l, b_l, c_l, d_l is given by

$$\Delta_l \boldsymbol{X} = \gamma_l \boldsymbol{Y} - \tfrac{1}{2}\xi\kappa\Phi_l \boldsymbol{Z}, \tag{24}$$

where $\boldsymbol{X} = \{a_l, b_l, c_l, d_l\}$, $\boldsymbol{Y} = \{\bar{a}_l, \bar{b}_l, \bar{c}_l, \bar{d}_l\}$, and $\boldsymbol{Z} = \{z_l^1, z_l^2, z_l^3, z_l^4\}$. The elements of the vectors are given in Table 2. If the motor is not self-propelled, the slip velocity does not exist. By taking $\kappa = 0$, we obtain $\boldsymbol{X} = \gamma_l \boldsymbol{Y}/\Delta_l$, which is the solutions for the motion of two linked spheres with the velocity V derived by Stimson and Jeffery.[13]

In the bispherical coordinate system,[13,16] the forces on individual spheres given in Eq. (7), and denoted here as F_1 at the S_1 sphere ($\eta = \eta_1$) and F_2 at the S_2 sphere ($\eta = \eta_2$), are given by

$$\begin{aligned}
F_1 &= \frac{2\sqrt{2}\pi\bar{\mu}}{\xi} \sum_{l=1}^{\infty} (2l+1)(a_l + b_l + c_l + d_l), \\
F_2 &= \frac{2\sqrt{2}\pi\bar{\mu}}{\xi} \sum_{l=1}^{\infty} (2l+1)(a_l - b_l + c_l - d_l).
\end{aligned} \tag{25}$$

Thus, the total force is

$$F_z = \frac{4\sqrt{2}\pi\bar{\mu}}{\xi} \sum_{l=1}^{\infty} (2l+1)(a_l + c_l). \tag{26}$$

From the force-free condition, $F_z = 0$, and Eq. (24), we can find the propulsion velocity of the dimer motor given in Eq. (8).

Table 2 The coefficients for the motor velocity in Eq. (8) and the fluid stream function in Eq. (24).

$$\begin{aligned}
\Phi_l &= -\frac{l(l+1)}{2(2l+1)}\{e^{(l-\frac{1}{2})\eta_2}A_{l-1} - (2\cosh\eta_2)e^{(l+\frac{1}{2})\eta_2}A_l + e^{(l+\frac{3}{2})\eta_2}A_{l+1} \\
&\quad + e^{-(l-\frac{1}{2})\eta_2}B_{l-1} - (2\cosh\eta_2)e^{-(l+\frac{1}{2})\eta_2}B_l + e^{-(l+\frac{3}{2})\eta_2}B_{l+1}\}, \\
\Delta_l &= 4\sinh^2(l+\tfrac{1}{2})(\eta_1-\eta_2) - (2l+1)^2\sinh^2(\eta_1-\eta_2), \\
f_l &= \xi^2 l(l+1)/\{\sqrt{2}(2l-1)(2l+1)(2l+3)\}, \\
\bar{a}_l &= (2l+3)\{4e^{-(l+\frac{1}{2})(\eta_1-\eta_2)}\sinh(l+\tfrac{1}{2})(\eta_1-\eta_2) \\
&\quad + (2l+1)^2 e^{(\eta_1-\eta_2)}\sinh(\eta_1-\eta_2) \\
&\quad + 2(2l-1)\sinh(l+\tfrac{1}{2})(\eta_1-\eta_2)\cosh(l+\tfrac{1}{2})(\eta_1+\eta_2) \\
&\quad - 2(2l+1)\sinh(l+\tfrac{3}{2})(\eta_1-\eta_2)\cosh(l-\tfrac{1}{2})(\eta_1+\eta_2) \\
&\quad - (2l+1)(2l-1)\sinh(\eta_1-\eta_2)\cosh(\eta_1+\eta_2)\}, \\
\bar{b}_l &= -(2l+3)\{2(2l-1)\sinh(l+\tfrac{1}{2})(\eta_1-\eta_2)\sinh(l+\tfrac{1}{2})(\eta_1+\eta_2) \\
&\quad - 2(2l+1)\sinh(l+\tfrac{3}{2})(\eta_1-\eta_2)\sinh(l-\tfrac{1}{2})(\eta_1+\eta_2) \\
&\quad + (2l+1)(2l-1)\sinh(\eta_1-\eta_2)\cosh(\eta_1+\eta_2)\}, \\
\bar{c}_l &= -(2l-1)\{4e^{-(l+\frac{1}{2})(\eta_1-\eta_2)}\sinh(l+\tfrac{1}{2})(\eta_1-\eta_2) \\
&\quad - (2l+1)^2 e^{-(\eta_1-\eta_2)}\sinh(\eta_1-\eta_2) \\
&\quad + 2(2l+1)\sinh(l-\tfrac{1}{2})(\eta_1-\eta_2)\cosh(l+\tfrac{3}{2})(\eta_1+\eta_2) \\
&\quad - 2(2l+3)\sinh(l+\tfrac{1}{2})(\eta_1-\eta_2)\cosh(l+\tfrac{1}{2})(\eta_1+\eta_2) \\
&\quad + (2l+1)(2l+3)\sinh(\eta_1-\eta_2)\cosh(\eta_1+\eta_2)\}, \\
\bar{d}_l &= (2l-1)\{2(2l+1)\sinh(l-\tfrac{1}{2})(\eta_1-\eta_2)\sinh(l+\tfrac{3}{2})(\eta_1+\eta_2) \\
&\quad - 2(2l+3)\sinh(l+\tfrac{1}{2})(\eta_1-\eta_2)\sinh(l+\tfrac{1}{2})(\eta_1+\eta_2) \\
&\quad + (2l+1)(2l+3)\sinh(\eta_1-\eta_2)\sinh(\eta_1+\eta_2)\}, \\
z_l^1 &= -(2l+3)\sinh(l-\tfrac{1}{2})\eta_1\cosh(l+\tfrac{3}{2})(\eta_1-\eta_2) \\
&\quad + (2l+3)\sinh(l-\tfrac{1}{2})\eta_2 \\
&\quad + (2l-1)\cosh(l-\tfrac{1}{2})\eta_1\sinh(l+\tfrac{3}{2})(\eta_1-\eta_2), \\
z_l^2 &= (2l+3)\cosh(l-\tfrac{1}{2})\eta_1\cosh(l+\tfrac{3}{2})(\eta_1-\eta_2) \\
&\quad - (2l+3)\cosh(l-\tfrac{1}{2})\eta_2 \\
&\quad - (2l-1)\sinh(l-\tfrac{1}{2})\eta_1\sinh(l+\tfrac{3}{2})(\eta_1-\eta_2), \\
z_l^3 &= (2l+3)\sinh(l-\tfrac{1}{2})(\eta_1-\eta_2)\cosh(l+\tfrac{3}{2})\eta_1 \\
&\quad + (2l-1)\sinh(l+\tfrac{3}{2})\eta_2 \\
&\quad - (2l-1)\cosh(l-\tfrac{1}{2})(\eta_1-\eta_2)\sinh(l+\tfrac{3}{2})\eta_1, \\
z_l^4 &= -(2l+3)\sinh(l-\tfrac{1}{2})(\eta_1-\eta_2)\sinh(l+\tfrac{3}{2})\eta_1 \\
&\quad - (2l-1)\cosh(l+\tfrac{3}{2})\eta_2 \\
&\quad + (2l-1)\cosh(l-\tfrac{1}{2})(\eta_1-\eta_2)\cosh(l+\tfrac{3}{2})\eta_1, \\
\Xi_l &= \tfrac{1}{2}(z_l^1 + z_l^3).
\end{aligned}$$

References

1 W. F. Paxton, K. C. Kistler, C. C. Olmeda, A. Sen, S. K. S. Angelo, Y. Cao, T. E. Mallouk, P. E. Lammert and V. H. Crespi, *J. Am. Chem. Soc.*, 2004, **126**, 13424.

2 G. A. Ozin, I. Manners, S. Fournier-Bidoz and A. Arsenault, *Adv. Mater.*, 2005, **17**, 3011.

3 J. Wang, *Nanomachines: Fundamentals and Applications*, Wiley-VCH, Weinheim, 2013.

4 R. A. L. Jones, *Soft Machines: Nanotechnology and Life*, Oxford University Press, Oxford, 2004.

5 R. Kapral, *J. Chem. Phys.*, 2013, **138**, 020901.

6 R. Golestanian, T. B. Liverpool and A. Ajdari, *New J. Phys.*, 2007, **9**, 126.

7 H. Ke, S. Ye, R. L. Carroll and K. Showalter, *J. Phys. Chem. A*, 2010, **114**, 5462.

8 I. Theurkauff, C. Cottin-Bizonne, J. Palacci, C. Ybert and L. Bocquet, *Phys. Rev. Lett.*, 2012, **108**, 268303.

9 S. Ebbens, D. A. Gregory, G. Dunderdale, J. R. Howse, Y. Ibrahim, T. B. Liverpool and R. Golestanian, *Europhys. Lett.*, 2014, **106**, 58003.

10 A. Brown and W. Poon, *Soft Matter*, 2014, **10**, 4016–4027.

11 G. Rückner and R. Kapral, *Phys. Rev. Lett.*, 2007, **98**, 150603.

12 L. F. Valadares, Y.-G. Tao, N. S. Zacharia, , V. Kitaev, F. Galembeck, R. Kapral and G. A. Ozin, *Small*, 2010, **6**, 565.

13 M. Stimson and G. B. Jeffery, *Proc. R. Soc. A*, 1926, **111**, 110–116.

14 M. N. Popescu, M. Tasinkevych and S. Dietrich, *Europhys. Lett.*, 2011, **95**, 28004.

15 P. M. Morse and H. Feshbach, *Methods of Theoretical Physics*, McGraw-Hill, New York, 1953.

16 J. Happel and H. Brenner, *Low Reynolds Number Hydrodynamics*, Noordhoff International publishing, Leyden, 1973.

17 B. V. Derjaguin and G. P. Sidorenkov, *Kolloidn. Zh.*, 1947, **9**, 335–347.

18 J. L. Anderson and D. C. Prieve, *Sep. Purif. Meth.*, 1984, **13**, 67–103.

19 J. L. Anderson, *Ann. Rev. Fluid Mech.*, 1989, **21**, 61–99.

20 R. Golestanian, T. B. Liverpool and A. Ajdari, *Phys. Rev. Lett.*, 2005, **94**, 220801.

21 A. Malevanets and R. Kapral, J. Chem. Phys., **110**, 8605 (1999); *ibid.*, **112**, 72609 (2000). For reviews, see, R. Kapral, Adv. Chem. Phys., **140**, 89 (2008); G. Gompper, T. Ihle, D. M. Kroll and R. G. Winkler, Adv. Polym. Sci., **221**, 1 (2009).

22 T. Ihle and D. M. Kroll, *Phys. Rev. E*, 2001, **63**, 020201(R).

23 Y.-G. Tao and R. Kapral, *J. Chem. Phys.*, 2008, **128**, 164518.

24 P. H. Colberg and R. Kapral, *EPL*, 2014, **106**, 30004.

25 M. Yang, A. Wysocki and M. Ripoll, *Soft Matter*, 2014, **10**, 6208.

26 J. P. Hernandez-Ortiz, P. T. Underhill and M. D. Graham, *J. Phys.: Condens. Matter*, 2009, **21**, 204107.

27 K. Drescher, R. E. Goldstein, N. Michel, M. Polin and I. Tuval, *Phys. Rev. Lett.*, 2010, **105**, 168101.

28 K. Drescher, J. Dunkel, L. H. Cisneros, S. Ganguly and R. E. Goldstein, *Proc. Natl. Acad. Sci. U.S.A.*, 2011, **108**, 10940–10945.

29 D. Saintillan and M. J. Shelley, *J. R. Soc. Interface*, 2012, **9**, 571.

30 S. Thakur and R. Kapral, *Phys. Rev. E*, 2012, **85**, 026121.

31 J. Schwarz-Linek, C. Valeriani, A. Cacciuto, M. E. Cates, D. Marenduzzo, A. N. Morozov and W. C. K. Poon, *PNAS*, 2012, **109**, 4052.

32 A. Zöttl and H. Stark, *Phys. Rev. Lett.*, 2014, **112**, 118101.

33 I. Gradshteyn and I. Ryzhik, *Table of integrals, Series, and Products*, Academic Press, New York, 7th edn, 2007.

34 S. Y. Reigh, *J. Chem. Phys.*, 2013, **139**, 194107.